Journal Name

Crossmark

PAPER

dd Month yyyy
REVISED
dd Month yyyy

Multivariate Time Series Classification of Fermi-Detected Gamma-Ray Transients Using Convolutional-Recurrent Neural Networks

Arpan Aryam John¹, Krushna Govind Shete¹, Shabnam Iyyani^{1,2,*} and Saptarshi Bej³

- ¹ School of Physics, Indian Institute of Science Education and Research Thiruvananthapuram, 695551, India
- ² Centre of High Performance Computing, Indian Institute of Science Education and Research Thiruvananthapuram, 695551, India
- 3 School of Data Science, Indian Institute of Science Education and Research Thiruvananthapuram, 695551, India
- *Author to whom any correspondence should be addressed.

E-mail: shabnam@iisertvm.ac.in

Keywords: High energy astrophysics, Gamma-ray astronomy, Deep Learning, Convolutional neural networks, Recurrent neural networks, LSTM

Abstract

Fermi Gamma-ray Space Telescope has detected a diverse range of gamma-ray transients since its launch in 2008. Over the years, Fermi has accumulated an extensive public archive of transient events. Traditional classification methods for these events typically rely on fixed thresholds, localisation accuracy, and characteristic light-curve features. However, in the current era of time-critical, multi-wavelength, and multi-messenger astronomy, rapid and reliable classification is essential to enable timely follow-up and coordinated observations.

In this work, we develop and present two deep learning-based classifiers that integrate convolutional and recurrent neural network architectures. Using multivariate time-series inputs derived from Fermi-GBM data, our models are trained to distinguish among four classes of gamma-ray transients: Gamma-Ray Bursts (GRBs), Terrestrial Gamma-ray Flashes (TGFs), Solar Flares (SFLAREs), and Soft Gamma Repeaters (SGRs). Furthermore, the models are designed to flag events that do not conform to any of these categories, providing a pathway for identifying potentially new or rare transient types. Training was conducted using a carefully curated subset of high-confidence Fermi events. The resulting models achieve an overall classification accuracy of 93%, and identify approximately 2.5% of the triggers as outliers of unknown origin. When applied to Fermi events with uncertain classifications, our models assign 60% of them to the TGF category with over 60% confidence.

These results demonstrate that incorporating deep learning-based classification into onboard or automated data pipelines can significantly enhance transient identification, minimize misclassification, and improve the discovery potential of new phenomena in future high-energy astrophysics missions.

1 Introduction

High energy gamma ray astrophysical transients are short-lived bursts of hard X-rays or gamma rays, that produce dramatic changes in intensity on time scales ranging from milliseconds to weeks. These are usually produced by the most extreme conditions in our universe, like massive stellar explosions, compact object mergers, magnetospheric reconnections in neutron stars, solar activities, etc, and, hence, are a tool for probing deep into the mechanisms behind our high energy Universe. Some of the extensively observed and studied gamma ray transients include Gamma Ray Bursts (GRBs, von Kienlin et al. 2020), Terrestrial Gamma-ray Flashes (TGFs, Roberts et al. 2018; Lindanger et al. 2020), Solar Flares (SFLAREs, Ackermann et al. 2014), Soft Gamma ray Repeaters (SGRs, Hurley 2011; Minaev et al. 2014) etc.

The Fermi Gamma-ray Space Telescope (Meegan et al., 2009), launched on June 11, 2008, is designed to study high-energy transients, particularly gamma-ray bursts (GRBs). It continuously

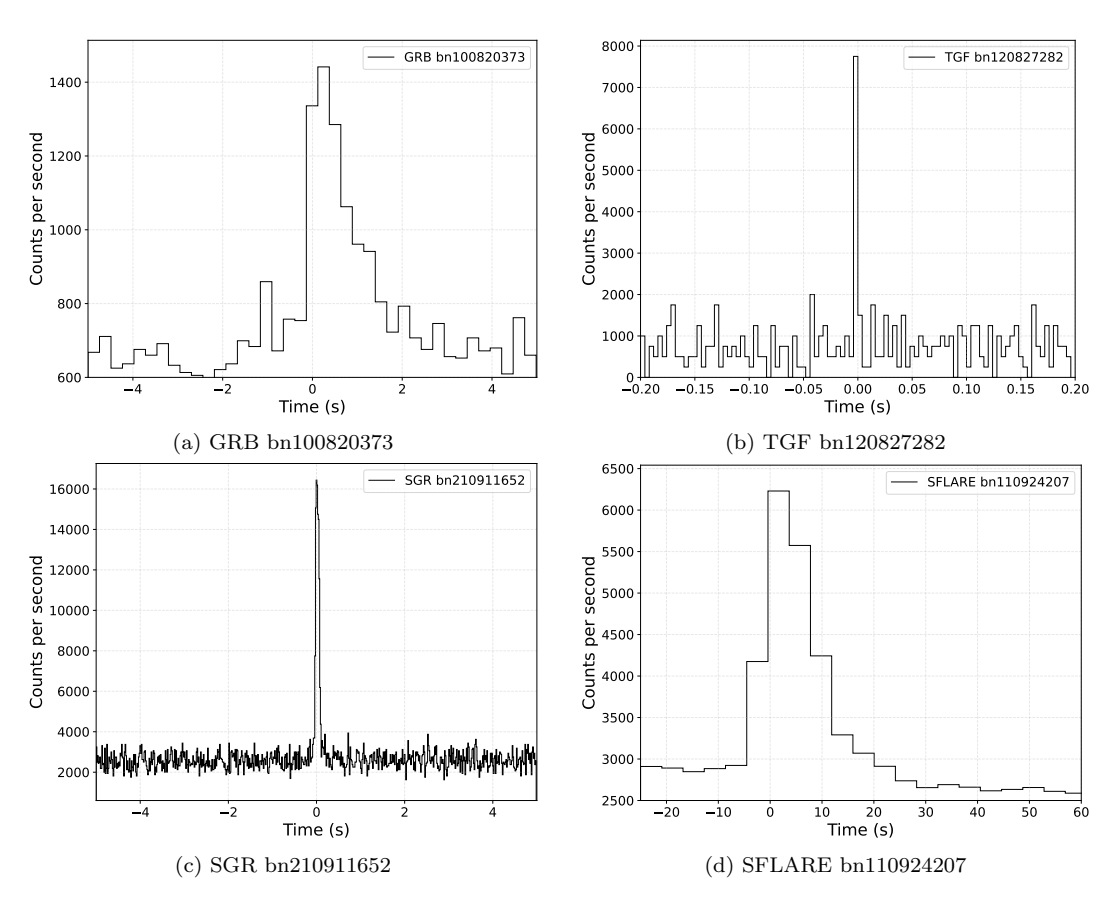


Figure 1: Examples of the lightcurves of different transient events, shown with different time bin sizes. (a) GRB bn100820373 with a bin size of 0.256 s in the 100–900 keV energy range, displaying a characteristic burst profile with rapid variability. (b) TGF bn120827282 with a bin size of 0.004 s in the 100–900 keV energy range, showing an extremely short-duration peak typical of terrestrial gamma—ray flashes. (c) SGR bn210911652 with a bin size of 0.016 s in the 10–100 keV energy range, exhibiting multiple short spikes, a signature of magnetar bursts. (d) SFLARE bn110924207 with a bin size of 4.096 s in the 10–100 keV energy range, highlighting a gradual rise and decay structure often seen in solar flares.

monitors nearly the entire sky across a broad energy range from a few keV to several MeV. An extensive open source database known of detected and classified triggers is publicly available.

The automatic classification of transients detected by Fermi Gamma ray Burst Monitor (GBM) currently follows a two-step process. The first step involves an onboard classification performed almost instantly (1-5s) by the flight software (Meegan et al., 2009). This system utilises a combination of event localisation, spectral hardness ratios, and McIlwain L-coordinates, applying Bayesian analysis to assign a probabilistic classification to each transient. In the second step, once the flight software is triggered, a subset of the event data is transmitted to ground-based centres, where further analysis and classification are conducted on the ground. The ground based analysis can take tens of seconds to a few minutes to complete (Thompson & Wilson-Hodge, 2024). In the era of multi-messenger astronomy, where transient events are often unpredictable and short-lived, rapid and accurate identification is critical to enable timely follow-up observations. Such swift classification facilitates coordinated observations across multiple observatories and wavelengths, as well as through different messenger channels like neutrinos and gravitational waves. Therefore, there is a pressing need for alternative, faster, and more efficient approaches to transient classification that can complement or enhance existing systems.

With the increasing availability of data, machine learning, particularly its subfield - deep learning, has gained substantial significance and application in astrophysics (Mcculloch & Pitts, 1943; Kembhavi & Pattnaik, 2022; Baron, 2019). The rapid advancement of Graphics Processing Unit (GPU) technology has substantially increased computational capacity, enabling the training of complex models on large datasets, which are now common in modern astronomical surveys. Deep learning algorithms, inspired by the architecture of the human brain, employ artificial neural networks (ANNs; Zhang 2000) to capture non-linear patterns in data. By stacking multiple

interconnected layers, these models automatically extract relevant features from raw inputs, minimising the need for manual feature engineering typically required in conventional machine learning approaches.

Two of the most commonly used deep learning architectures are convolutional neural networks (CNNs; LeCun et al. 2015) and recurrent neural networks (RNNs), each offering distinct advantages depending on the nature of the data. CNNs are particularly suited for extracting local and spatial features and have been widely used in astronomical tasks involving image-based data, including the classification of objects in the Optical Gravitational Lensing Experiment (OGLE; Monsalves, N. et al. 2024), galaxy morphology prediction (Dieleman et al., 2015), transient detection in sky surveys (Cabrera-Vives et al., 2017), and star-galaxy classification (Bertin, E. & Arnouts, S., 1996).

RNNs, on the other hand, are designed to handle sequential data and excel in capturing temporal dependencies, making them especially effective for time-series applications where the order of data points holds crucial information. They have been applied in astrophysics for tasks such as redshift estimation (Luo et al., 2024), solar flare prediction (Liu et al., 2019), and GRB light curve reconstruction (Manchanda et al., 2024).

In this study, we developed and evaluated two deep learning models, based on combination of CNNs and RNNs architectures but differing in their structural design and approach, for multiclass transient classification using Fermi-GBM data. Both models use multivariate time-series inputs derived from transient light curves binned at different time resolutions. The first model integrates convolutional and recurrent layers sequentially, while the second model employs multiple parallel convolutional branches for each time binning resolution, followed by a shared recurrent layer to capture temporal dependencies. Our approach builds upon prior studies such as Abraham et al. 2021, which demonstrated that transient classes exhibit distinctive light curve morphologies(Figure 1) that can be exploited for classification, and Peng Zhang et al. 2024 used CNNs for binary GRB/non-GRB classification based on count maps. While works like Dimple et al. 2024 have employed Uniform Manifold Approximation and Projection with Principal Component Analysis to cluster GRBs using their lightcurves.

Expanding on this foundation, we apply R-CNNs for the first time to a four-class problem involving GRBs, TGFs, SGRs and SFLAREs, achieving high classification accuracy with computational efficiency. The CNN models are particularly effective in capturing local features and characteristic temporal patterns within short time bins, enabling fast inference. In contrast, RNN models leverage the sequential nature of time-series data to capture long-term dependencies and evolution patterns within light curves. By using these approaches in two different combined fashions, we systematically explore their individual strengths and demonstrate their complementary capabilities in accurately classifying high-energy transients, as well as in identifying potential outlier events indicative of rare or unknown phenomena.

The paper is organised as follows: in Section 2, we describe the data collection process and pre-processing steps. Section 3 details the methodology and the architectures employed in the two R-CNN model approaches. The results of our analysis are presented in Section 4. In section 5, we discuss about the misclassified events and the model limitations, the relevance of our work in the context of previous studies, its applicability to real-time classification, and the treatment of uncertain or outlier events with potential discovery prospects. Finally, section 6 provides a summary of our findings.

2 Data

This section outlines the procedures for data collection, preprocessing, and dataset balancing to ensure optimal model performance.

2.1 Data Collection

The data used in this study is obtained from the Fermi Gamma-Ray Space Telescope, operated by NASA and publicly available through the High Energy Astrophysics Science Archive Research Center (HEASARC). Fermi is designed to detect gamma-ray bursts (GRBs) and other high-energy hard X-ray and gamma ray astrophysical phenomena. It carries two primary instruments: the Gamma-ray Burst Monitor (GBM), which includes 12 Sodium Iodide (NaI) detectors covering 8 keV to 900 keV and 2 Bismuth Germanate (BGO) detectors covering 250 keV to 40 MeV, and the Large Area Telescope (LAT), which operates in the higher energy range of 30 MeV to 300 GeV. In this work, we use only GBM data, as it is responsible for triggering event detections, while LAT emission is observed for only a small fraction of cases.

The NaI detectors on GBM are oriented such as to provide near-complete sky coverage, excluding only the Earth-occulted region. Beyond detection, GBM also provides spectral

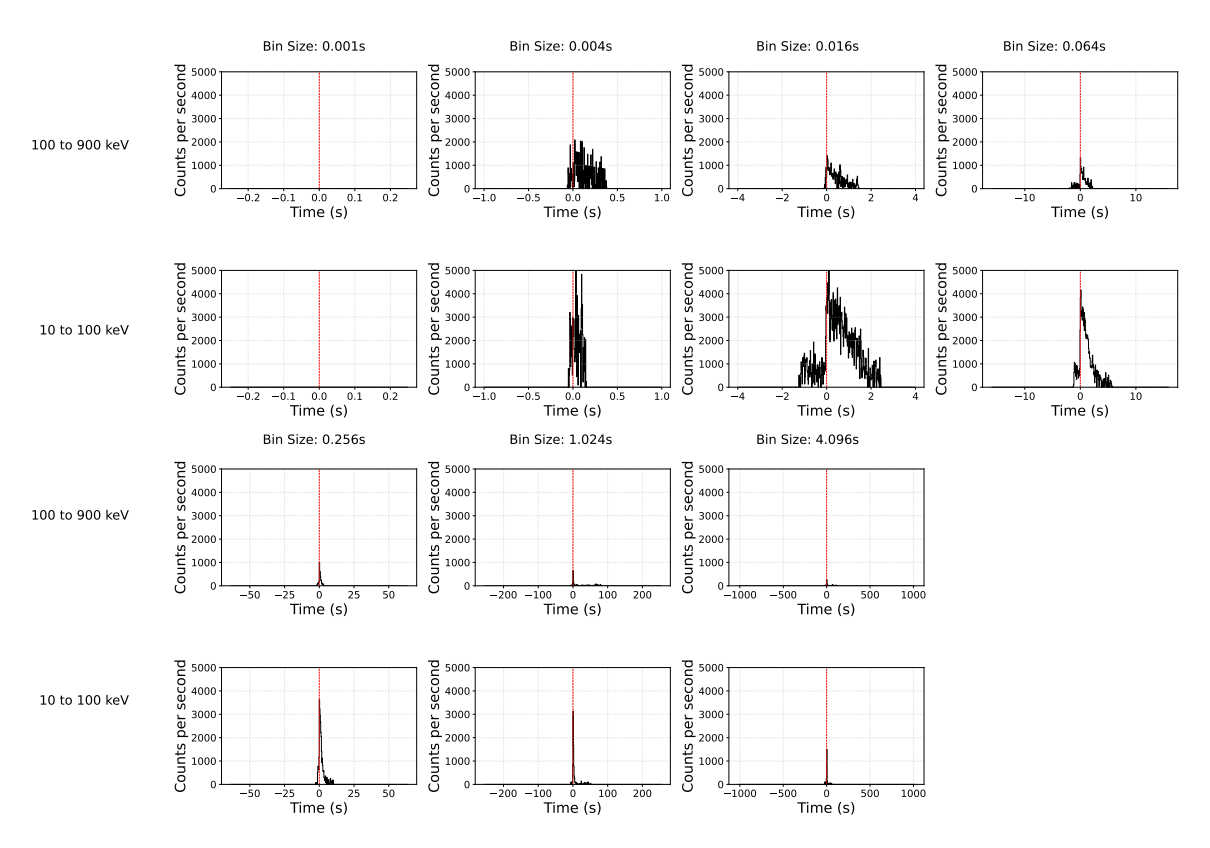


Figure 2: The background-subtracted light curves used as model inputs are shown above. Each sample comprises 14 light curves from two energy ranges (10–100 keV and 100–900 keV) and seven time-bin resolutions. When the algorithm fails to clearly separate signal from background, an empty light curve is passed to the model.

information and real-time localisation of these transients. This rapid localisation enables re-pointing of the LAT detector and facilitates coordinated multi-wavelength follow-up observations by ground-based observatories, communicated through GCN Circulars.

The Data Processing Unit (DPU) onboard *Fermi* produces three types of data packets: CTIME, CSPEC, and TTE (Meegan et al., 2009). For this study, only the TTE (Time-Tagged Event) files were used, specifically those from the top brighter NaI detectors (highest number of photon counts) with an angular separation of less than 60° from the burst location. The TTE data provides the highest spectral and temporal resolution available, offering 128 energy channels and a temporal resolution of 2 microseconds. This makes TTE data ideally suited for detailed time-series analysis of high-energy transient events.

From the Fermi GBM Trigger Catalog (FermiGTRIG¹), only triggers with 100% classification probability as assigned by the GBM flight software (Meegan et al., 2009) were selected for this study. This probability reflects the confidence level in the classification of each trigger as per the flight software (Meegan et al., 2009). Based on this selection criterion, a total of 1000 GRBs, 1000 TGFs, 1000 SFLAREs, and 492 SGRs were identified.

2.2 Data Preprocessing

The TTE data primarily contain two key pieces of information: the detection time and the energy of each photon. By binning the photon detection times from the TTE file, a counts per second versus time plot is generated. This is referred to as the light curve of the transient. Since the light curve captures the temporal evolution of photon counts, it is treated as time series data.

The typical durations of high-energy transients span a wide range, from sub-millisecond for TGFs (Mailyan et al., 2020) and about 0.01–1 s for SGRs (Göğüş et al., 2001), to roughly 0.1–100 s for GRBs (von Kienlin et al., 2020), and several minutes to hours for SFLAREs (Reep & Knizhnik, 2019). Therefore, the detectability of transients in light curve analysis is governed by their intrinsic timescales, as different transient durations achieve optimal signal-to-noise ratios (SNR; $> 4\sigma$ in given energy ranges; von Kienlin et al. 2020) at different time binnings (Figure 2). To account for

https://heasarc.gsfc.nasa.gov/w3browse/Fermi/Fermigtrig.html

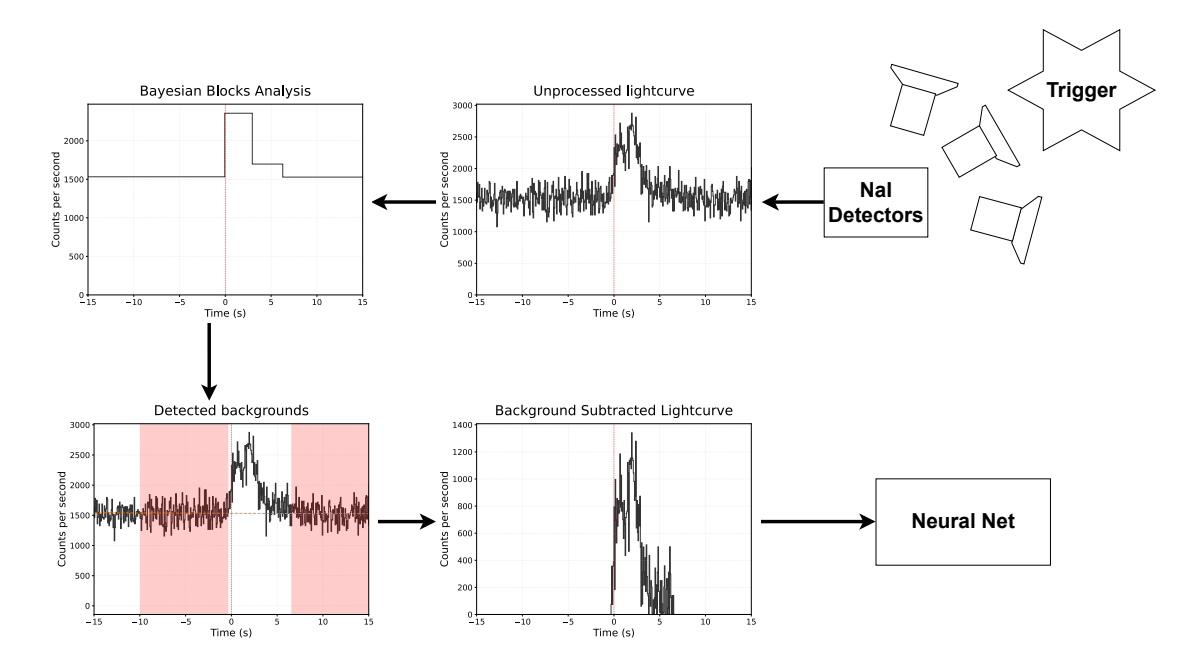


Figure 3: Schematic illustration of the data processing pipeline, showing the complete workflow from data extraction to background removal and generation of clean data arrays.

this variability, a single binning scheme was insufficient to capture the diversity of the transient signals. A detailed analysis of light curves from various transient classes allowed the identification of seven optimal bin sizes - 0.001 s, 0.004 s, 0.016 s, 0.064 s, 0.256 s, 1.024 s, and 4.096 s - chosen to maximise the SNR across different event types.

For each trigger, the three brightest TTE files from the NaI detectors closest to the source direction were selected and combined to create light curves in two energy ranges: 10–100 keV (channels 3–50) and 100–900 keV (channels 51–124) (Figure 2). The subsequent analysis was performed separately for each energy range. The photon arrival times² were first adjusted by subtracting the trigger time, effectively setting the trigger time to zero.

For each of the seven bin sizes, the bin edges were calculated using the following equations:

Starting time = trigger time -
$$(dno \times r \times i)$$
,
Stopping time = trigger time + $(dno \times (1 - r) \times i)$,

where dno=500 is the total number of bin edges, r is the ratio of pre-trigger to post-trigger bins, and i is the bin size. When the counts in the TTE files did not fully span the defined time range, some bins were only partially populated. To ensure consistency, such bins were excluded, and the light curves were padded by replacing the non-zero counts at the extremes with zeros, effectively limiting each light curve to 500 bins centered around the trigger time.

Following this, the Bayesian block algorithm (Scargle et al., 2013) with a false alarm probability $(p_0 = 0.01)$ was applied to each light curve allowing to identify the start and stop times of each transient, as well as facilitated the identification of pre- and post-transient background regions in each light curve. The schematic diagram depicting the data processing is shown in Figure 3. We further note that if the Bayesian block analysis detected only two time blocks, or if the interval between the extreme blocks (representing the background regions) was too short relative to the bin size, the event was identified as lacking a significant signal for that particular binning and energy range. If this occurs we send an array with zero signal to prevent the network learning from data without significant signal in that specific time binning and energy range.

The background was modeled using a polynomial fit (up to the fourth order was investigated) in the identified pre and post transient time intervals. The best fit was identified using reduced chi-square closest to 1. Subsequently, the polynomial was subtracted from the lightcurve. This procedure was repeated across all seven binnings and both energy ranges.

As a result, for each trigger, a total of 14 background-subtracted light curves were generated (seven bin sizes \times two energy bands). Each light curve was formatted as a time series with two

²The arrival times of the photons and the trigger time of the burst are reported in Mission Elapsed Time (MET) which for *Fermi* is the number of seconds since 00:00:00 UTC on January 1, 2001 (UTC).

feature channels (representing the two energy ranges), resulting in an array shape of (samples, 499, 2), where the number of samples varied depending on the specific dataset under analysis. This standardised multi-resolution and multi-energy representation ensured that both temporal structures and spectral hardness information were preserved for input into the machine learning models.

For approximately 5% of the triggers in our initial dataset, this method fails to detect a signal in any of the studied time binning or energy intervals. These triggers are therefore excluded from the training and test sets (Table 1). The characteristics of these events are discussed in Section 5.3.

Partition	No. of GRBs	No. of TGFs	No. of SGRs	No. of SFLAREs
Total	990	866	477	974
Train	790	691	387	776
Test	200	175	90	198

Table 1: The final size of data set used for training and testing the models are give above.

For the first deep learning model, R-ConvNet, the histogram counts from different bin sizes were stacked into a single array. These arrays were then concatenated to form a three-dimensional input of shape (samples, channels, time steps), where each channel corresponds to a specific bin size. The model was trained using inputs of shape (channels, time steps), allowing it to capture variability and patterns across multiple temporal resolutions for each event.

In the second deep learning, MI-DCL (Multi Input - Dual Channel Lightcurve), a similar approach was followed; however, instead of stacking the histogram counts into a single array, each bin size was treated as a separate input. Seven distinct input layers corresponding to the seven bin sizes were fed into the model and merged into a single tensor via concatenation. This design enabled the model to process each time resolution independently before combining the extracted features.

2.3 Data Balancing and splitting

A holdout strategy was employed to split the dataset into training, validation, and test sets. The identified dataset (as mentioned in section 2.1) was first divided into training and test sets, with a portion of the training set further set aside for validation during model training. The model was trained on the remaining training data, while the validation set was used to monitor performance after each epoch and to fine- tune hyperparameters. Finally, once training was complete, the model's performance was evaluated on the test set, which remained unseen during both training and validation.

A distinct validation set was maintained, separate from the test set, to prevent data leakage during training and to ensure an unbiased assessment of the model's generalisation performance. Specifically, out of the identified datasets we used around 800 samples each of GRBs, TGFs, and SFLAREs, and 400 samples of SGRs for training, while 20% of this training set was allocated for validation. The test set comprised roughly 200 samples each of GRBs, TGFs, and SFLAREs, and 92 samples of SGRs. This approach ensured a balanced distribution of classes across training, validation, and test datasets.

3 Methodology

3.1 Neural Networks

Artificial Neural Networks (ANNs) are a class of machine learning techniques designed to identify underlying patterns in data. ANNs aim to mimic biological neural systems through the use of multilayer perceptrons, where multiple neural layers are stacked and interconnected. Each layer in an ANN comprises numerous neurons, which serve as the fundamental processing units. These interconnected neurons form a complex network, with each neuron having its own set of weights (\mathbf{W}) and biases (\mathbf{b}) . For a given input vector, each layer produces an output vector (\mathbf{z}) according to the relation

$$\mathbf{z}^{[l]} = \mathbf{W}^{[l]} \cdot \mathbf{a}^{[l-1]} + \mathbf{b}^{[l]},\tag{1}$$

where I represents the Ith layer and $\mathbf{a}^{[l-1]}$ is the activation (output) vector from the previous $(l-1)^{th}$ layer as it serves as the input to the current layer. The result is then passed through a non-linear activation function before being propagated to the next layer. Activation functions are crucial as they introduce non-linearity into the network, enabling it to learn complex and non-linear patterns. This process is repeated across all layers of the network. While the same activation function is often used throughout the network, the final output layer typically employs a

task-specific activation function; for instance, sigmoid is used for binary classification tasks, while softmax or linear activations are employed for multi-class classification. The entire process of taking inputs, transforming them through layers, and producing an output is known as forward propagation. The model then calculates the error between its predicted output and the true labels using loss functions such as Mean Squared Error (MSE), Cross-Entropy Loss, or Hinge Loss. The training objective is to minimise this error, which is achieved through back-propagation. During back-propagation, the weights and biases of each neuron are updated to reduce the loss using gradient descent, with the gradients of the loss function computed as follows:

$$\mathbf{W}^{l} = \mathbf{W}^{l} - \alpha \frac{\partial L}{\partial \mathbf{W}^{l}},$$

$$\mathbf{b}^{l} = \mathbf{b}^{l} - \alpha \frac{\partial L}{\partial \mathbf{b}^{l}}.$$
(2)

where α is learning rate, L is the loss function while $\frac{\partial L}{\partial \mathbf{W}^l}$ and $\frac{\partial L}{\partial \mathbf{b}^l}$ represent the gradients of the loss with respect to weights and biases in the layer l respectively. This process is repeated iteratively across multiple training epochs to optimise model performance. It is important to note that while forward propagation is always used in ANNs, backward propagation is only applied during training.

Convolutional Neural Networks (CNNs) extend the standard ANN architecture by incorporating convolutional and pooling layers. In CNNs, the convolutional layer applies a filter to the input data to extract meaningful features by moving across the input with a fixed step size (stride) and creating feature maps. This is typically followed by pooling layers, commonly max-pooling, which reduce the dimensionality of the feature maps while preserving important information. Depending on the data type, one can use 1D, 2D, or 3D convolutional layers. CNNs are adept at learning spatial patterns and are particularly useful in identifying both local and hierarchical features. For example, in the case of 1D time-series data such as transient light curves, CNNs treat the temporal axis as a spatial dimension, allowing the network to recognise features like sudden spikes or spectral hardness variations. Each subsequent layer in the CNN hierarchy learns increasingly abstract representations, making CNNs highly effective in extracting complex patterns while filtering out noise. CNNs employ both forward and backward propagation during training.

Recurrent Neural Networks (RNNs), introduced in 1985 (Hinton et al., 2012), are specifically designed for sequential and time-series data. Unlike standard ANNs, where each input is processed independently, RNNs are capable of retaining context from previous inputs, making them well-suited for modeling sequences where current outputs depend on prior states. This is achieved by introducing a hidden state that carries information forward through the sequence. The output at each time step (zt) is given by

$$\mathbf{z}t = \mathbf{W}h \cdot \mathbf{h}t - 1 + \mathbf{W}x \cdot \mathbf{x}t + \mathbf{b},\tag{3}$$

where the hidden state $\mathbf{h}t-1$ incorporates information from previous time steps, $\mathbf{x}t$ is input vector at the current time step, while $\mathbf{W}h$ determines how much of the previous hidden state ht-1 influences the current output and $\mathbf{W}x$ determines how much of the current input x_t contributes to the current output. This recurrent connection provides a memory component that is absent in standard feed-forward ANNs (see Equation (1)). RNNs use back-propagation through time to compute gradients across all time steps and update weights accordingly. In this study, we utilise Long Short-Term Memory (LSTM) networks, a specialised form of RNN proposed by Hochreiter & Schmidhuber (1997), designed to overcome challenges such as vanishing gradients in long sequences. LSTM networks introduce memory cells regulated by three gates - input, forget, and output gates - that determine which information to retain, discard, or output at each step. This mechanism enables LSTMs to capture long-term dependencies within sequences effectively. Given that our dataset consists of time-series photon count data, LSTMs are well-suited to capturing hidden temporal patterns essential for accurate transient classification.

3.2 Neural Network Architecture

Our team developed two R-CNN models with distinct architectures. The main distinguishing feature of the two R-CNNs was how they handled the heterogeneous nature of the data due to different bin sizes.

3.2.1 R-ConvNet In the first model, the data is first passed through a convolutional input layer. This layer applies a set of filters (kernels) to extract low-level features from the input data. Following the initial convolution, a max-pooling layer is employed to reduce the spatial

dimensionality of the feature maps, thereby decreasing the number of learnable parameters and mitigating overfitting.

Subsequently, an additional convolutional layer is added, followed by an LSTM (Long Short-Term Memory) layer, with a max-pooling layer in between. This architecture allows the model to capture both spatial and temporal dependencies in the data—where convolutional layers focus on extracting local features, and LSTM layers capture sequential patterns. After these layers, a global max-pooling layer is applied, which operates similarly to standard max pooling but aggregates over the entire time axis, enabling the model to handle variable-length inputs.

The pooled output is then flattened and passed through a series of fully connected dense layers, which further learn high-level representations and patterns from the extracted features. Except for the output layer, each layer uses the ReLU (Rectified Linear Unit) activation function (Nair & Hinton, 2010), which is computationally efficient and helps mitigate the vanishing gradient problem. ReLU is defined mathematically as:

$$f(x) = \max(0, x). \tag{4}$$

Following the dense layers, three fully connected layers are included with dropout layers placed in between to prevent overfitting by randomly deactivating a fraction of neurons during training (Hinton et al., 2012). The final output layer uses a softmax activation function, appropriate for multi-class classification tasks, which converts the model outputs into probability distributions over the classes. The softmax function is given by:

$$Softmax(z_i) = \frac{e^{z_i}}{\sum_{j=1}^{C} e^{z_j}},\tag{5}$$

where C is the number of classes and z_i is the logit (input) to the softmax for class i.

Additionally, L2 regularisation is applied to all convolutional and dense layers to further prevent overfitting by penalising large weight values, which also stabilises the loss curve. Model training is performed using the Adam (Adaptive Moment Estimation) optimiser (Kingma & Ba, 2015), which adaptively adjusts the learning rate during training. The loss function used is categorical cross-entropy, standard for multi-class classification, and is defined as:

$$L(y, \hat{y}) = -\sum_{i=1}^{C} y_i \log(\hat{y}_i),$$
 (6)

where y_i is the true label and \hat{y}_i is the predicted probability for class i. This loss function quantifies the difference between the predicted and true distributions, guiding the model to make accurate predictions. The default EarlyStopping and ReduceLROnPlateau callbacks in keras are integrated to monitor the validation loss. EarlyStopping stops training if the loss doesn't improve for a fixed number of epochs, while ReduceLROnPlateau reduces the learning rate under same condition. The schematic representation of the model architecture is shown in Figure 4.

3.2.2 Multi-Input Dual Channel Lightcurve (MI-DCL) model. The second R-CNN model, referred to as the Multi-Input Dual Channel Lightcurve (MI-DCL) model, employs separate input branches for each bin size. Each of the seven light curve inputs is processed through an independent pathway. The input format follows the time series structure of the light curves, with two features representing photon counts in the two energy bands: 10–100 keV and 100–900 keV.

Each input branch consists of a one-dimensional convolutional layer with four filters of size 16, followed by a max-pooling layer with a pool size of 4. The output is then flattened and passed through a fully connected layer with 512 neurons activated by the ReLU function, as defined in equation 4. To mitigate overfitting, a dropout layer with a dropout rate of 0.25 is applied. This structure is replicated independently across all seven light curve inputs.

The extracted features from all seven branches are then concatenated into a single merged feature vector. This vector is reshaped into a two-dimensional tensor and passed through a Long Short-Term Memory (LSTM) layer comprising 256 units, with both dropout and recurrent dropout rates set at 0.3 to further reduce overfitting and improve generalization.

Subsequent to the LSTM layer, the architecture includes a dense layer with 1024 neurons and ReLU activation, followed by a dropout layer with a 0.5 dropout rate. This is followed by another dense layer with 512 neurons and ReLU activation, again accompanied by a dropout layer with a rate of 0.5. Finally, a softmax output layer, as described in equation 5, is used to produce class probabilities across four transient classes.

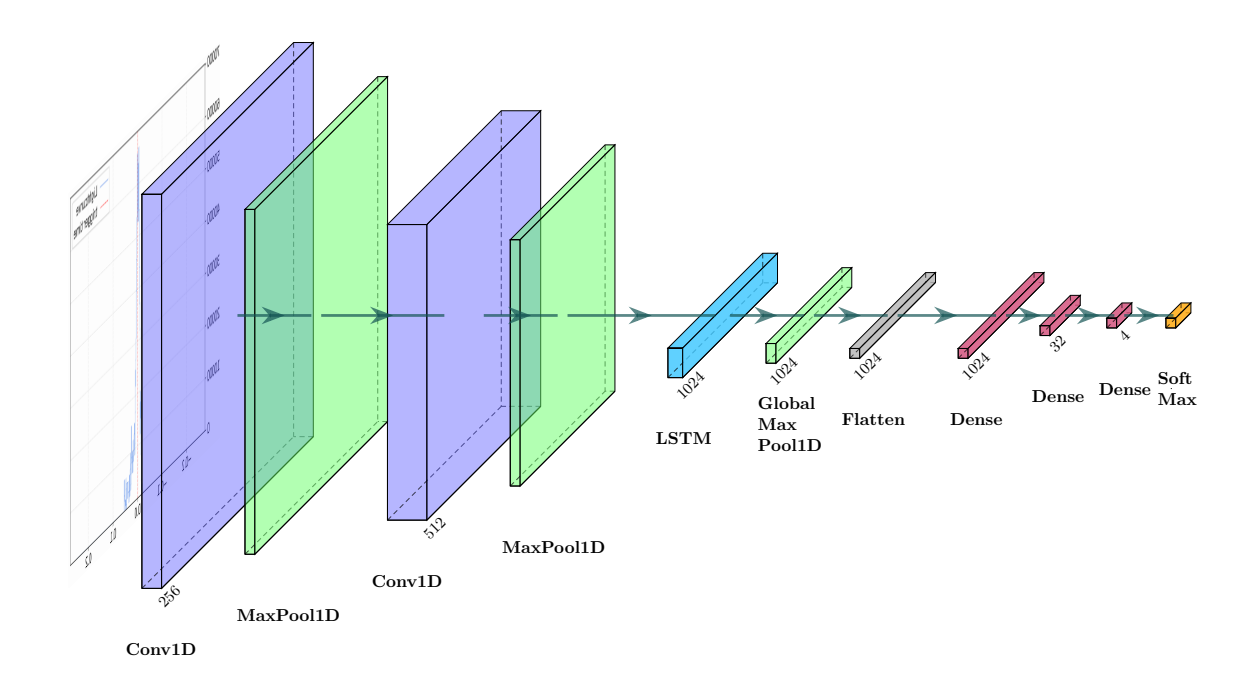


Figure 4: The schematic diagram of the proposed R-ConvNet model illustrates the detailed architecture, showing how the input data are processed through successive layers to learn underlying spatial and temporal features.

The model is optimised using the Adam optimiser with a learning rate of 0.0005 and $\beta_1 = 0.9$ (exponential decay rate for the first moment estimates). A learning rate scheduler is implemented to reduce the learning rate by a factor of 0.5 if the validation loss plateaus for three consecutive epochs, with a minimum learning rate capped at 1×10^{-6} . Additionally, a custom early stopping mechanism is employed: training halts if the model achieves a training accuracy of 95% or higher and maintains this performance for three consecutive epochs. This approach ensures efficient training, reducing unnecessary computation and mitigating overfitting risks. The loss function used is categorical cross-entropy, defined by equation 6.

The schematic diagram of the model architecture is provided in Figure 5. Overall, this architecture effectively combines convolutional feature extraction with temporal sequence modeling, enabling the model to capture both spectral and temporal characteristics of transient light curves. The MI-DCL model achieves robust multi-class classification performance across diverse transient types and was trained for a total of 88 epochs.

4 Results

Two R-CNN models were developed and evaluated using both built-in methods in Keras and custom-built functions. Model performance was assessed on the test set, with the learning curves presented in Figure 6. To comprehensively assess the performance of our models, we evaluated them using four standard metrics: Accuracy, Precision, Recall, and F1-score (Sasaki et al., 2007). Accuracy measures the overall proportion of correctly classified instances. However, because our dataset is imbalanced, meaning some transient classes (e.g. SGRs) are underrepresented compared to others (e.g. GRBs), accuracy alone can provide an incomplete or even misleading picture of model performance. To address this, we additionally report Precision, which quantifies the proportion of correctly predicted positive instances out of all positive predictions made by the model, and Recall, which measures how many actual positive instances are correctly identified. The F1-score, defined as the harmonic mean of Precision and Recall, balances both metrics and offers a single robust indicator of model performance, especially in cases of class imbalance. By incorporating these complementary metrics alongside accuracy, we ensure a more reliable and transparent evaluation of our classification models, particularly in the context of uneven class distributions where rare transients can be easily misclassified if only accuracy is considered.

The classification reports for both models, including Accuracy, Precision, Recall, and F1-score, are summarised in Table 2. Both models achieved a comparable overall accuracy of 93%, successfully classifying the majority of events into their correct categories, with some degree of misclassification visible in the confusion matrices (Figure 7).

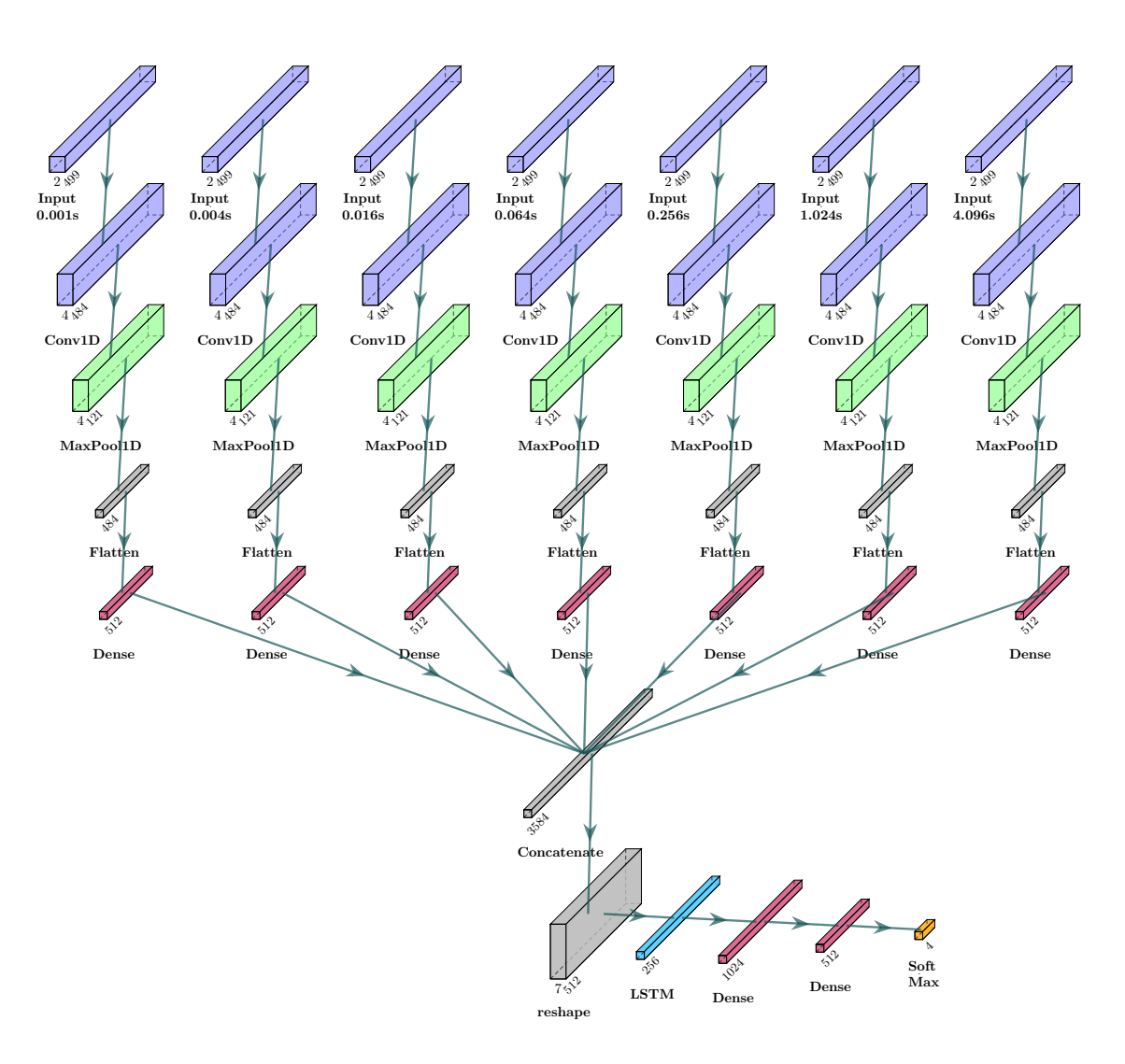


Figure 5: The schematic diagram of the proposed MI-DCL model illustrates the detailed architecture and how the input data are processed through successive layers to learn underlying spatial and temporal features.

Model	Class	Precision	Recall	F1-Score	Accuracy (overall)
R-ConvNet	GRB	0.94	0.94	0.94	
	TGF	0.91	0.99	0.95	0.93
	SGR	0.94	0.90	0.92	
	SFLARE	0.95	0.88	0.91	
MI-DCL	GRB	0.94	0.91	0.92	
	TGF	0.93	0.98	0.95	0.93
	SGR	0.95	0.91	0.93	
	SFLARE	0.91	0.92	0.92	

Table 2: The classification report for both the R-ConvNet and MI-DCL models on transient classification are give above. The table includes the precision, recall and F1-score for each class of transient: GRB, TGF, SGR, and SFLARE along with the overall Accuracy of each model. Both models show consistently high scores and balanced precision and recall.

To account for instances in the test data that do not closely resemble any of the trained classes, we introduced a fifth class, labelled "UNCERTAIN" shortened to "UNCERT". This allows the model to flag events that differ significantly from the known classes, based on their classification confidence. Specifically, if the softmax confidence for all classes falls below 60% (refer Appendix A for more details), we categorise that instance under the UNCERTAIN class, effectively treating it as dissimilar to any of the trained categories. This strategy enables the model to handle out-of-distribution or ambiguous events, providing a practical mechanism for identifying potentially novel

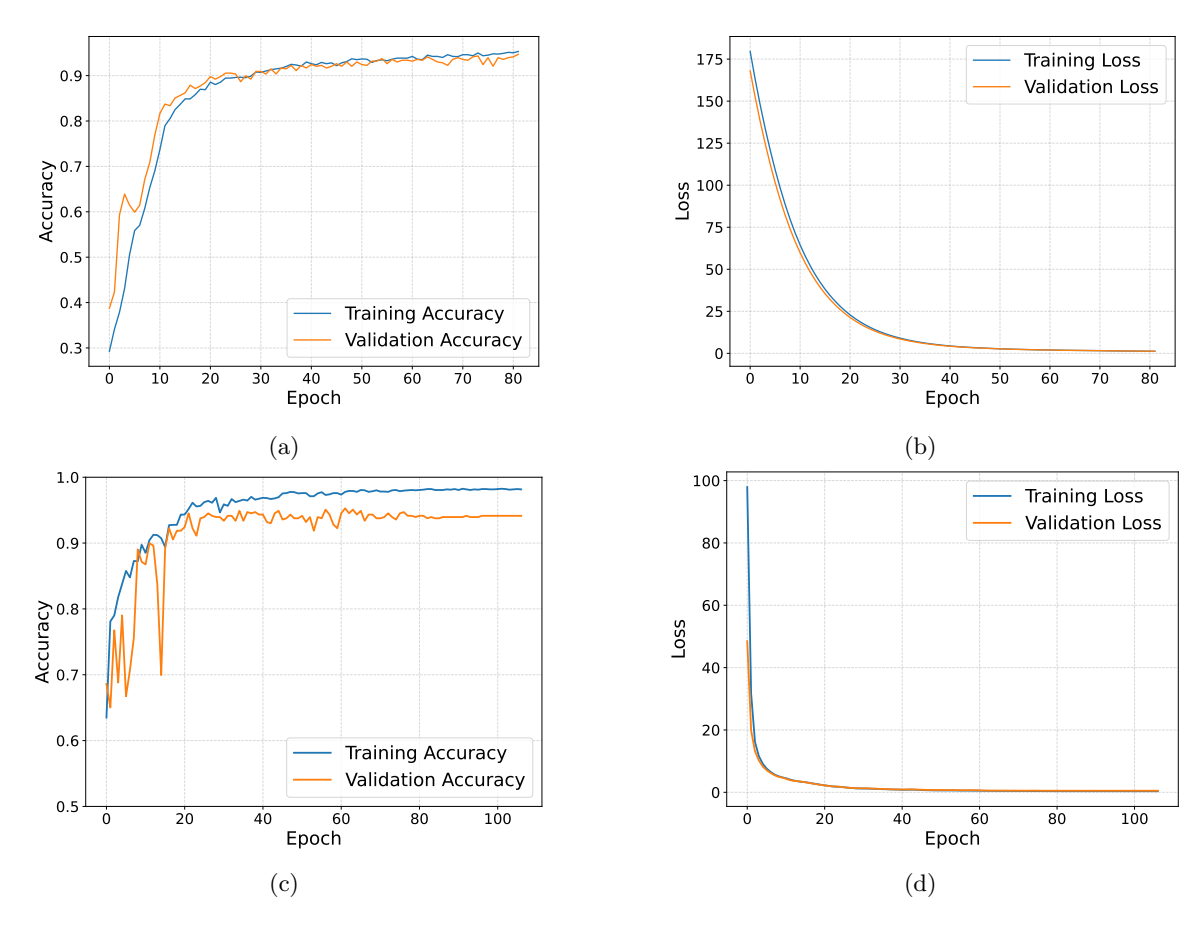


Figure 6: The training performance of our deep learning models for transient classification is shown above. Panels (a) and (c) present the accuracy—epoch curves for the MI-DCL and R-ConvNet models, respectively, while panels (b) and (d) display the corresponding loss—epoch curves. The steady decrease and subsequent stabilization of both training and validation losses indicate that the models generalize well and are not prone to overfitting, despite the relatively limited dataset.

or misclassified transients. To illustrate the impact of this approach, we present two sets of confusion matrices: the standard four-class classification without the uncertainty filter, and the expanded five-class classification after applying the confidence threshold (Figure 7). This comparison highlights how the model performs both with and without the incorporation of the uncertainty criterion. Both our models classified around 1.4%(MI-DCL) and 2.00%(R-ConvNet) of the test data into the uncertain class.

Continuing from the above results, we further examined the classification performance by visualising the learned feature representations using two-dimensional UMAP (Uniform Manifold Approximation and Projection; McInnes et al. 2018) projections for both models. Figure 8 shows the UMAP plots for the MI-DCL model (panel a) and the R-ConvNet model (panel b). These visualisations provide an intuitive understanding of how well the models are able to distinguish between different transient classes in the high-dimensional feature space. Events correctly classified by the models are represented by distinct colours corresponding to their true class labels (GRB, TGF, SGR, and SFLARE), while misclassified events are marked in purple, and events classified as UNCERTAIN are shown in brown. The clustering observed in the UMAP plots indicates that both models effectively capture the distinguishing features of each transient class. Notably, the UNCERTAIN events predominantly appear near the boundaries of these clusters, reflecting regions where the model finds it challenging to make confident predictions. This further validates the utility of the uncertainty class in identifying ambiguous or out-of-distribution samples.

5 Discussion

5.1 Analysis of Misclassified Events and Model Limitations

Despite the overall strong performance of our models, achieving over 93% accuracy, some instances of misclassification were consistently observed. A detailed inspection of these misclassified cases revealed several contributing factors. One of the main causes of uncertain classifications appears to

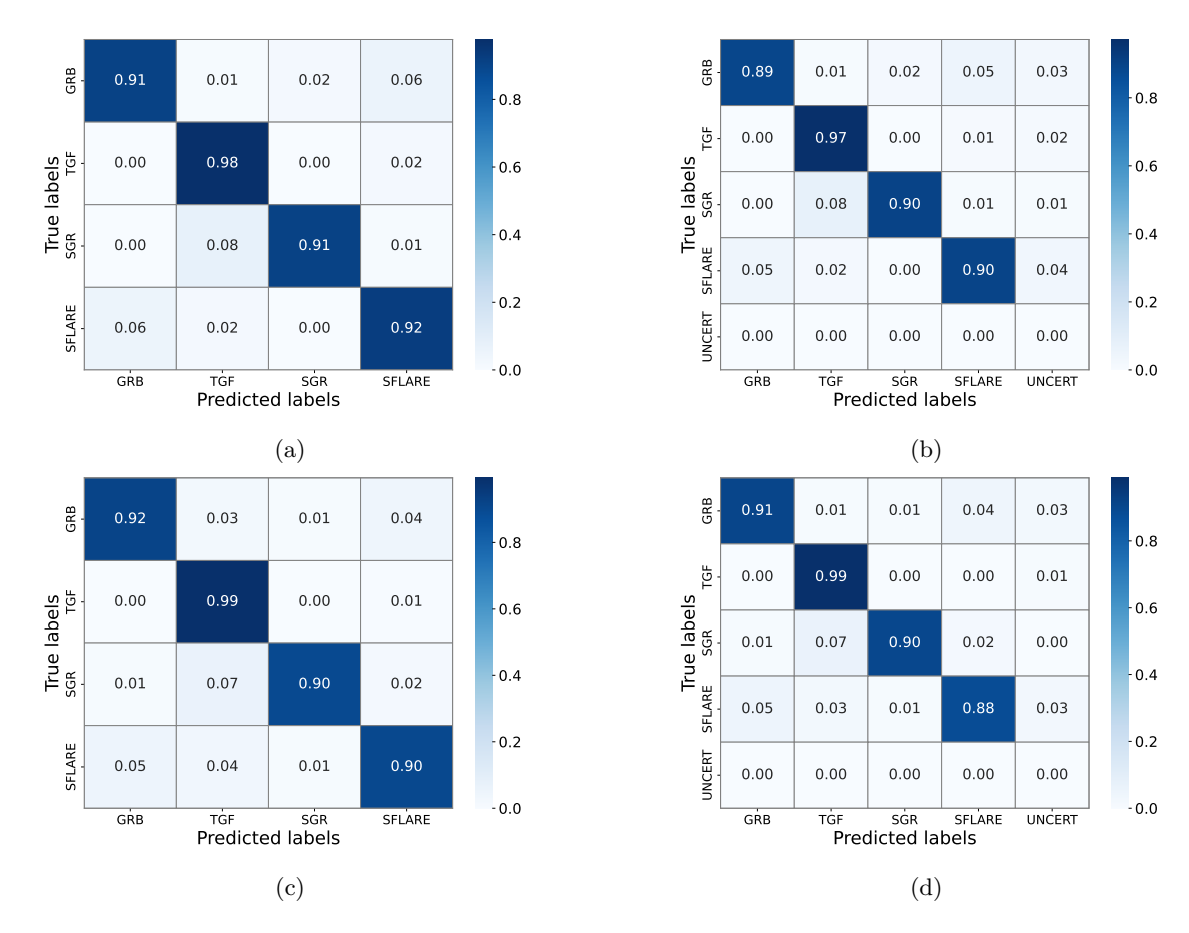


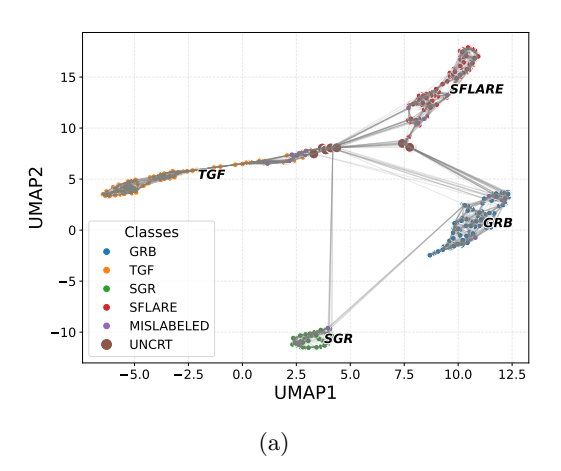
Figure 7: Confusion matrices of both MI-DCL [(a), (b)] and R-ConvNet [(c), (d)] models on test data. (a) and (c) show the standard confusion matrices, displaying classification performance for GRBs, TGFs, SGRs, and SFLAREs. (b) and (d) include classifications with an additional 'UNCERT' category.

be weak signal strength ($< 2\sigma$), where the transient does not produce a sufficiently strong count rate within the selected energy ranges, making it difficult for the model to distinguish it from other classes (Figure 10a). Additionally, some events with dominant emission in the MeV range become unclassifiable due to our chosen NaI detectors which is restricted till 900 keV (Figure 10b). Uncertainties can also arise from inconsistent backgrounds or signals not centered on the trigger (Figure 10c). In such cases, the triggering signal may represent a weak precursor, while the main high-count event occurs several seconds later—beyond the time window selected by our current algorithm.

Another source of misclassification was the occurrence of atypical light curve patterns that did not conform to the typical temporal morphology seen in their respective classes. For example, certain GRBs exhibited extended emission (higher T90 durations) that overlapped with typical SFLARE durations, leading to occasional misclassification between these two classes. Similarly, some SGR events with shorter, sharper profiles were misidentified as TGFs, owing to their overlapping short-duration features and comparable count structures in the binned light curves.

Our analysis also suggests that class imbalance, particularly the relatively smaller number of SGR events in the training data, might have contributed to reduced classification robustness for this class. Increasing the volume and diversity of training examples for underrepresented classes, especially SGRs, would likely improve classification fidelity.

Lastly, we note that our current model architecture is based solely on time-series photon counts in two energy bands. The addition of contextual features, such as localisation information (Right Ascension and Declination), could potentially help resolve classification ambiguities. This is particularly applicable for classes like SFLARE and TGF, which are confined to specific astrophysical or geophysical origins, unlike GRBs which are isotropic. Incorporating such auxiliary features in future model iterations may improve the classification accuracy further, particularly in cases where light curve morphology alone is insufficient to distinguish between classes.



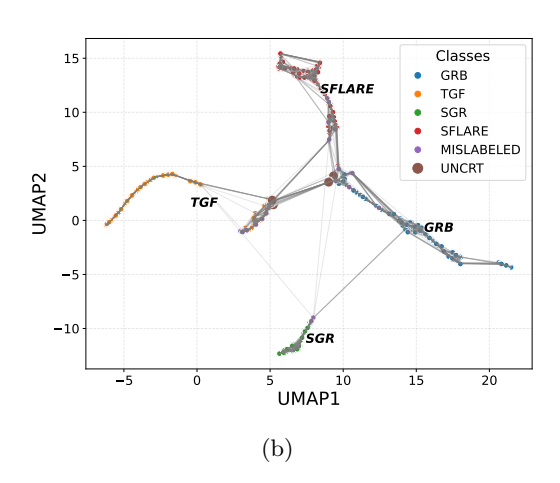


Figure 8: Two-dimensional UMAP visualization of (a) MI-DCL model and (b) R-ConvNet model for multiclass classification of transient light curves from the *Fermi* GBM telescope. The learnt data representation was extracted from the penultimate hidden layers of each model. The plots display correctly classified transients (GRB - blue, TGF - orange, SGR - green, SFLARE - red), mislabeled events (purple), and uncertain events (brown). Each transient class forms distinct clusters, demonstrating the model's ability to separate different classes effectively. As expected, uncertain events tend to lie near cluster boundaries, indicating regions of higher classification ambiguity.

5.2 Comparison with Existing Classification Strategies

Existing classification methods on Fermi-GBM rely on threshold-based algorithms, which are efficient but can miss weak or atypical events. Apart from this there were some efforts to identify the GRB using machine learning and neural networks. Dimple et al. (2024) used DBSCAN clustering and Dynamic Time Warping to detect GRB from the AstroSat CZTI data; their module showed the capability to identify both long and short types of GRBs. While the module enhanced the fast automated GRB detection, it is used only for GRB detection and not for any other transients. The model is less sensitive to the short GRBs, and additionally, there is a trade-off between the template bank size and DTW computation efficiency.

A model proposed by Peng Zhang et al. (2024) adopts a similar approach to ours. Their CNN-based framework uses count maps from the 12 NaI detectors for binary GRB classification, considering all energy channels. They developed three architectures—plain CNN, ResNet, and ResNet-CBAM—each trained with time resolutions of 64, 128, and 256 ms over a 120 s window. By generating count maps from each triggered NaI detector, they expanded their GRB dataset from 3083 to 6330 samples. The non-GRB set, drawn from 120 s segments of Fermi GBM background data, comprised 10000 randomly selected examples from 40000 candidates. Their training, validation, and test sets contained 3082/6000, 1507/2000, and 1741/2000 GRB/non-GRB samples, respectively. The best performing model, ResNet-CBAM (64 ms), achieved 96.57% accuracy, which increased to 96.81% after model fusion.

Furthermore, Abraham et al. 2021 developed an ML-based method for automated detection of GRB candidates in the 60–250 keV range using AstroSat CZTI data. Their approach applied density-based spatial clustering to identify excess power, followed by unsupervised hierarchical clustering to classify distinct light-curve patterns.

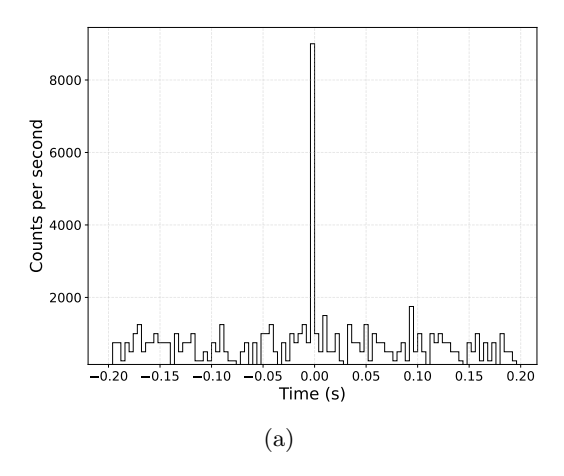
Thus, several deep learning approaches have been developed to classify events within a specific transient type, such as GRBs, or to distinguish particular trigger types from others. However, a framework that classifies multiple kinds of high-energy transients directly from time-series data while also identifying ambiguous or potentially novel events remains largely unexplored. The current work, thus, addresses to bridge this gap.

5.3 Computational Efficiency and Resource Utilisation

Our models take a very short time for training, within 1 minute using the P100 GPUs on Kaggle³. And for any new transient data instance, it can predict the class under 0.05 seconds. We have used the free GPU (GPU P100) provided by Kaggle Notebooks⁴ to train our models, which has reduced our model training time significantly. The current Flight Software generates classifications within 1–5 seconds (Meegan et al., 2009), whereas our neural network models can produce predictions in

³https://www.kaggle.com/

⁴https://www.kaggle.com/docs/notebooks/



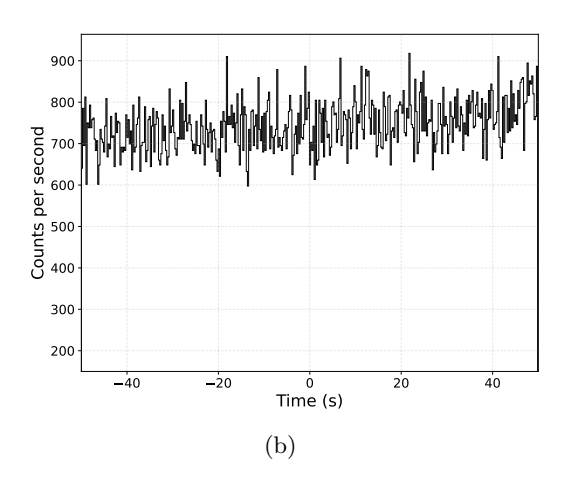


Figure 9: The lightcurves of a few triggers which were unclassified by *Fermi* GBM are shown above. (a) UNCERT bn191025926, however, got classified as TGF by both R-ConvNet and MI-DCL (100-900keV plot) models. (b) UNCERT bn220108026 was unclassified by R-ConvNet (100-900keV plot). No signal was clear in any time and energy binning.

about 0.1 seconds once the data are prepared. At present, preprocessing in Python takes nearly 1.5 seconds (CPU - AMD Ryzen 5 3550H), but this overhead could be significantly reduced through optimization or by implementing the pipeline in a faster language such as C/C++.

Occasionally, the data processing fails to identify a signal. This can be because the signal is not clearly visible in the chosen energy ranges (10-100 keV and 100-900 keV) or the signal is displaced from the trigger time. These abnormalities could be accounted for using a more complex algorithm in future works. For now these do not constitute a significant part of the data set and are hence neglected.

5.4 Interpretation of Uncertainty Classes Reported by Fermi and our models. In the Fermi GBM trigger catalogue, approximately 6% of the data remains unclassified, as the GBM flight software could not confidently assign these events to any known transient category. To assess the performance of our models on this ambiguous dataset, we applied our models to 50 of these unclassified events. MI-DCL provided a confident (0.6) prediction for all these events, while R-ConvNet failed to classify 7 of these events and interestingly, a majority of the data, around 60% is getting classified as TGF by both models. The lightcurves of some of these triggers are shown in Figure 9. This shows the potential for these neural network models to help classify this data when the Fermi GBM's methods fail. Even if the prediction is not always right it provides a good starting point for future investigation of the trigger.

In our classification model, the fifth category labeled 'UNCERT' serves as a safeguard against forcing low confidence predictions (softmax < 0.6) into one of the four known transient classes, thus providing a quantitative measure of classification reliability. The incorporation of the UNCERTAIN class proved insightful. By applying this thresholding mechanism, we were able to segregate ambiguous or novel events that did not exhibit sufficient similarity to any of the four trained classes. This approach reduces false positives in the primary classes and offers a systematic method to flag anomalous or outlier events.

A closer examination of events classified under the UNCERTAIN category revealed that a subset of these cases exhibited extremely low signal strengths, while others showed unusual or atypical temporal profiles, such as a highly varying background or an uncentred peak with respect to the trigger time (Figure 10a and 10c). Additionally, some events may correspond to transient phenomena not represented within our training set. This underscores the utility of the UNCERTAIN class as an effective tool for flagging outliers, highlighting anomalous behaviour, and potentially uncovering either rare or entirely new types of high-energy transients, as well as exceptional cases within known transient classes. Focused follow-up analyses of these UNCERTAIN events could offer valuable insights into the broader diversity and underlying complexity of transient populations observed by Fermi GBM.

6 Summary

To summarize, we have developed and implemented two R-CNN based deep learning models for the supervised classification of four major types of high energy transients: GRBs, TGFs, SGRs, and

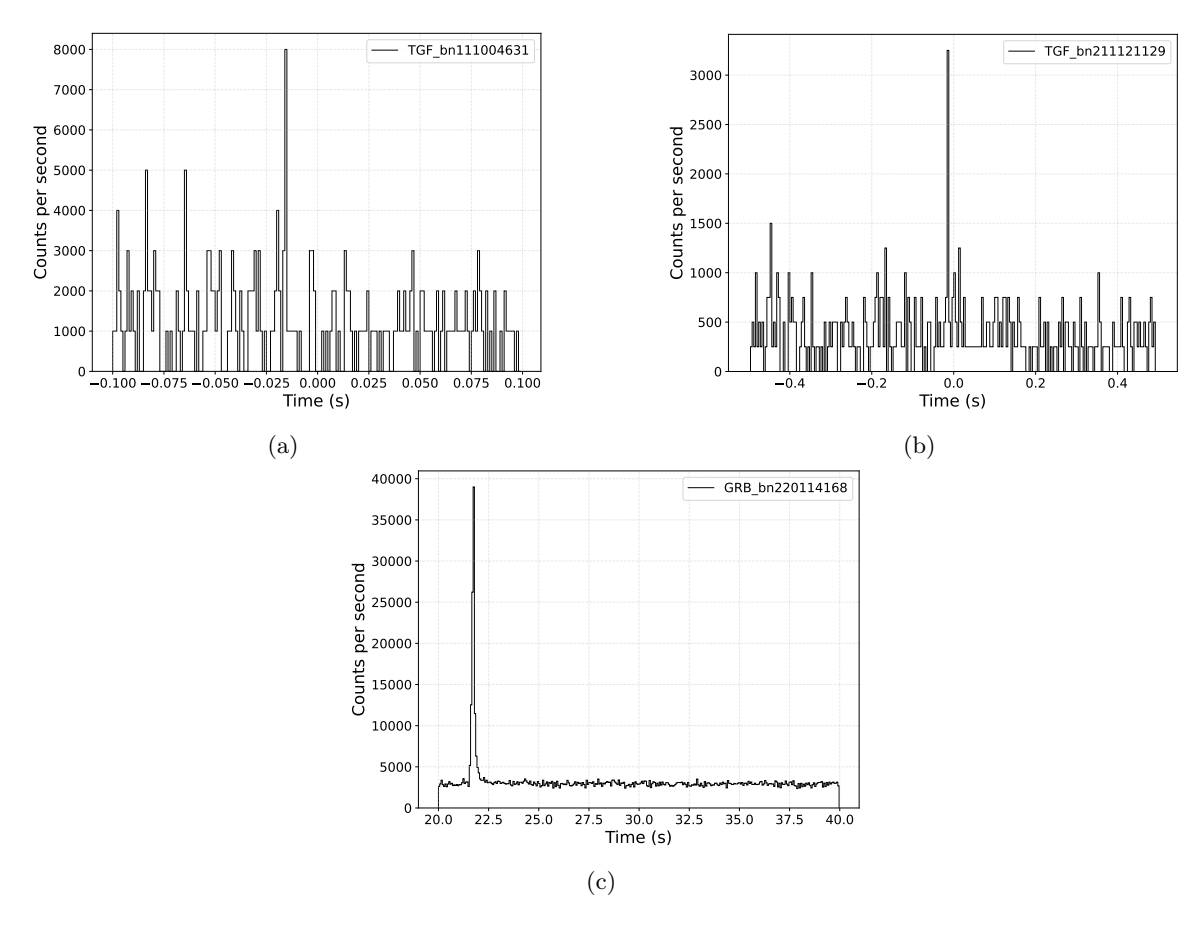


Figure 10: Our deep learning models failed to identify the above type of events. (a) The above TGF's signal is somewhat visible only in the energy band 40 - 240 keV (shown above) not in the energy ranges chosen for study; (b) This event is visible only in the 1-2 MeV (shown above) while our study is restricted to NaI whose energy range is till 900 keV only; (c) This GRB has its brightest signal occurring nearly 20s after the trigger time.

SFLAREs, using time series light curve data from the Fermi Gamma-ray Space Telescope.

Both models achieved an overall accuracy of approximately 93%, with minimal misclassification. A fifth 'uncertain' category was introduced for events with softmax confidence helps 60% across all algebrase accounting for about 1.2% of the test data. LIMAR visualizations

below 60% across all classes, accounting for about 1–2% of the test data. UMAP visualizations reveal that these uncertain events predominantly lie near the cluster boundaries of different trigger types, reflecting their inherent ambiguity.

This work thus presents two complementary deep learning frameworks capable of classifying diverse high energy transients directly from time series data while identifying ambiguous or potentially novel events. With an efficient processing time of only ~ 1.55 seconds per event, these models has the potential to be integrated into future observation pipelines to enable rapid classification and facilitate timely, coordinated multi-wavelength and multi-messenger follow-ups of high energy transients.

Acknowledgments

This research has made use of *Fermi* data obtained through High Energy Astrophysics Science Archive Research Center Online Service, provided by the NASA/Goddard Space Flight Center. This work utilized various software such as 3ML, NAIMA, PYTHON (Van Rossum & Drake Jr 1995), ASTROPY (Astropy Collaboration et al. 2013, 2018, 2022), NUMPY (Harris et al. 2020), SCIPY (Virtanen et al. 2020), MATPLOTLIB (Hunter 2007), FTOOLS (Blackburn 1995), Tensorflow (Abadi et al. 2015) etc. This research utilized computational resources made available through Kaggle's cloud infrastructure.

Funding

S.I. is supported by DST INSPIRE Faculty Scheme (IFA19-PH245) and SERB SRG Grant (SRG/2022/000211).

Author contributions

S.I conceived the study, designed the methodology, and supervised the overall research. The model development and data processing were carried out by A.A.J and K.G.S contributed to data analysis and visualization. A.A.J, K.G.S and S.I interpreted the results and prepared the manuscript. S.B. provided expert guidance on machine learning and deep learning methods, contributed to model evaluation, and assisted in refining the analysis and interpretation of results. All authors reviewed and approved the final version of the paper.

References

Abadi, M., Agarwal, A., Barham, P., et al. 2015, TensorFlow: Large-Scale Machine Learning on Heterogeneous Systems. https://www.tensorflow.org/

Abraham, S., Mukund, N., Vibhute, A., et al. 2021, Monthly Notices of the Royal Astronomical Society, 504, 3084, doi:10.1093/mnras/stab1082

Ackermann, M., Ajello, M., Albert, A., et al. 2014, ApJ, 787, 15, doi:10.1088/0004-637X/787/1/15

Astropy Collaboration, Robitaille, T. P., Tollerud, E. J., et al. 2013, A&A, 558, A33, doi:10.1051/0004-6361/201322068

Astropy Collaboration, Price-Whelan, A. M., Sipőcz, B. M., et al. 2018, AJ, 156, 123, doi:10.3847/1538-3881/aabc4f

Astropy Collaboration, Price-Whelan, A. M., Lim, P. L., et al. 2022, ApJ, 935, 167, doi:10.3847/1538-4357/ac7c74

Baron, D. 2019, arXiv: Instrumentation and Methods for Astrophysics. https://api.semanticscholar.org/CorpusID:119302873

Bertin, E., & Arnouts, S. 1996, Astron. Astrophys. Suppl. Ser., 117, 393, doi:10.1051/aas:1996164

Blackburn, J. 1995, in Astronomical Data Analysis Software and Systems IV, Vol. 77, 367

Cabrera-Vives, G., Reyes, I., Förster, F., Estévez, P. A., & Maureira, J.-C. 2017, The Astrophysical Journal, 836, 97, doi:10.3847/1538-4357/836/1/97

Dieleman, S., Willett, K. W., & Dambre, J. 2015, Monthly Notices of the Royal Astronomical Society, 450, 1441, doi:10.1093/mnras/stv632

Dimple, Misra, K., & Arun, K. G. 2024, ApJ, 974, 55, doi:10.3847/1538-4357/ad6d6a

Göğüş, E., Kouveliotou, C., Woods, P. M., et al. 2001, ApJ, 558, 228, doi:10.1086/322463

Harris, C. R., Millman, K. J., van der Walt, S. J., et al. 2020, Nature, 585, 357, doi:10.1038/s41586-020-2649-2

Hinton, G. E., Srivastava, N., Krizhevsky, A., Sutskever, I., & Salakhutdinov, R. 2012, ArXiv, abs/1207.0580. https://api.semanticscholar.org/CorpusID:14832074

Hochreiter, S., & Schmidhuber, J. 1997, Neural Computation, 9, 1735, doi:10.1162/neco.1997.9.8.1735

Hunter, J. D. 2007, Computing in Science & Engineering, 9, 90, doi:10.1109/MCSE.2007.55

Hurley, K. 2011, Advances in Space Research, 47, 1326, doi:https://doi.org/10.1016/j.asr.2010.03.001

Kembhavi, A., & Pattnaik, R. 2022, Journal of Astrophysics and Astronomy, 43, 1–10, doi:10.1007/s12036-022-09871-2

Kingma, D. P., & Ba, J. 2015, in 3rd International Conference on Learning Representations, ICLR 2015, San Diego, CA, USA, May 7-9, 2015, Conference Track Proceedings, ed. Y. Bengio & Y. LeCun. http://arxiv.org/abs/1412.6980

LeCun, Y., Bengio, Y., & Hinton, G. 2015, nature, 521, 436

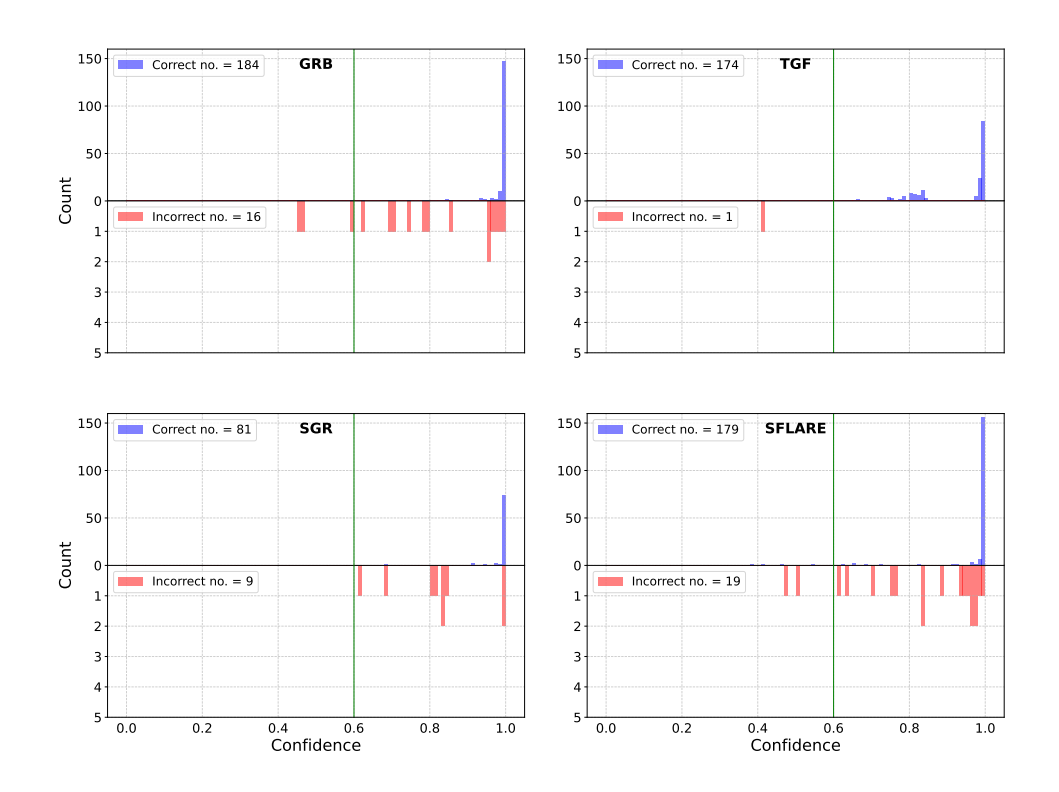
Lindanger, A., Marisaldi, M., Maiorana, C., et al. 2020, Journal of Geophysical Research (Atmospheres), 125, e31985, doi:10.1029/2019JD031985

- Liu, H., Liu, C., Wang, J. T. L., & Wang, H. 2019, The Astrophysical Journal, 877, 121, doi:10.3847/1538-4357/ab1b3c
- Luo, Z., Li, Y., Lu, J., et al. 2024, Monthly Notices of the Royal Astronomical Society, 535, 1844, doi:10.1093/mnras/stae2446
- Mailyan, B. G., Nag, A., Dwyer, J. R., et al. 2020, Scientific Reports, 10, 7286, doi:10.1038/s41598-020-63437-2
- Manchanda, A., Dainotti, M. G., Deepu, A., et al. 2024. https://arxiv.org/abs/2412.20091
- Mcculloch, W. S., & Pitts, W. H. 1943, Bulletin of Mathematical Biophysics, 5, 115
- McInnes, L., Healy, J., Saul, N., & Großberger, L. 2018, Journal of Open Source Software, 3, 861, doi:10.21105/joss.00861
- Meegan, C., Lichti, G., Bhat, P. N., et al. 2009, The Astrophysical Journal, 702, 791, doi:10.1088/0004-637X/702/1/791
- Minaev, P. Y., Pozanenko, A. S., Molkov, S. V., & Grebenev, S. A. 2014, Astronomy Letters, 40, 235, doi:10.1134/S106377371405003X
- Monsalves, N., Jaque Arancibia, M., Bayo, A., et al. 2024, A&A, 691, A106, doi:10.1051/0004-6361/202449995
- Nair, V., & Hinton, G. E. 2010, in Proceedings of the 27th international conference on machine learning (ICML-10), 807–814
- Peng Zhang, B. L., et al. 2024, The Astrophysical Journal Supplement Series, 272, 4
- Reep, J. W., & Knizhnik, K. J. 2019, ApJ, 874, 157, doi:10.3847/1538-4357/ab0ae7
- Roberts, O. J., Fitzpatrick, G., Stanbro, M., et al. 2018, Journal of Geophysical Research (Space Physics), 123, 4381, doi:10.1029/2017JA024837
- Sasaki, Y., et al. 2007, URL: https://www.cs. odu. edu/mukka/cs795sum09dm/Lecturenotes/Day3/F-measure-YS-26Oct07. pdf [accessed 2021-05-26], 49
- Scargle, J. D., Norris, J. P., Jackson, B., & Chiang, J. 2013, The Astrophysical Journal, 764, 167
- Thompson, D. J., & Wilson-Hodge, C. A. 2024, in Handbook of X-ray and Gamma-ray Astrophysics (Springer), 2383–2413
- Van Rossum, G., & Drake Jr, F. L. 1995, Python reference manual (Centrum voor Wiskunde en Informatica Amsterdam)
- Virtanen, P., Gommers, R., Oliphant, T. E., et al. 2020, Nature Methods, 17, 261, doi:10.1038/s41592-019-0686-2
- von Kienlin, A., Meegan, C. A., Paciesas, W. S., et al. 2020, ApJ, 893, 46, doi:10.3847/1538-4357/ab7a18
- Zhang, G. 2000, IEEE Transactions on Systems, Man, and Cybernetics, Part C (Applications and Reviews), 30, 451, doi:10.1109/5326.897072

A Appendix: Threshold Selection

We selected a threshold value of 60% based on the distribution of classification confidences (i.e softmax confidence obtained for each classification) shown in Figure 11. Most data points were classified with high confidence, typically in the 80–90% range. However, setting a higher threshold (e.g. 70–80%) would risk labeling genuinely confident predictions as uncertain. Conversely, a lower threshold (e.g. 40–50%) could result in incorrectly treating uncertain or confused predictions as confident classifications. Therefore, adopting a conservative threshold of 60% provides a reasonable balance, minimizing the mislabeling of both uncertain and confident instances.

(a) R-ConvNet confidence distribution



(b) MI-DCL confidence distribution

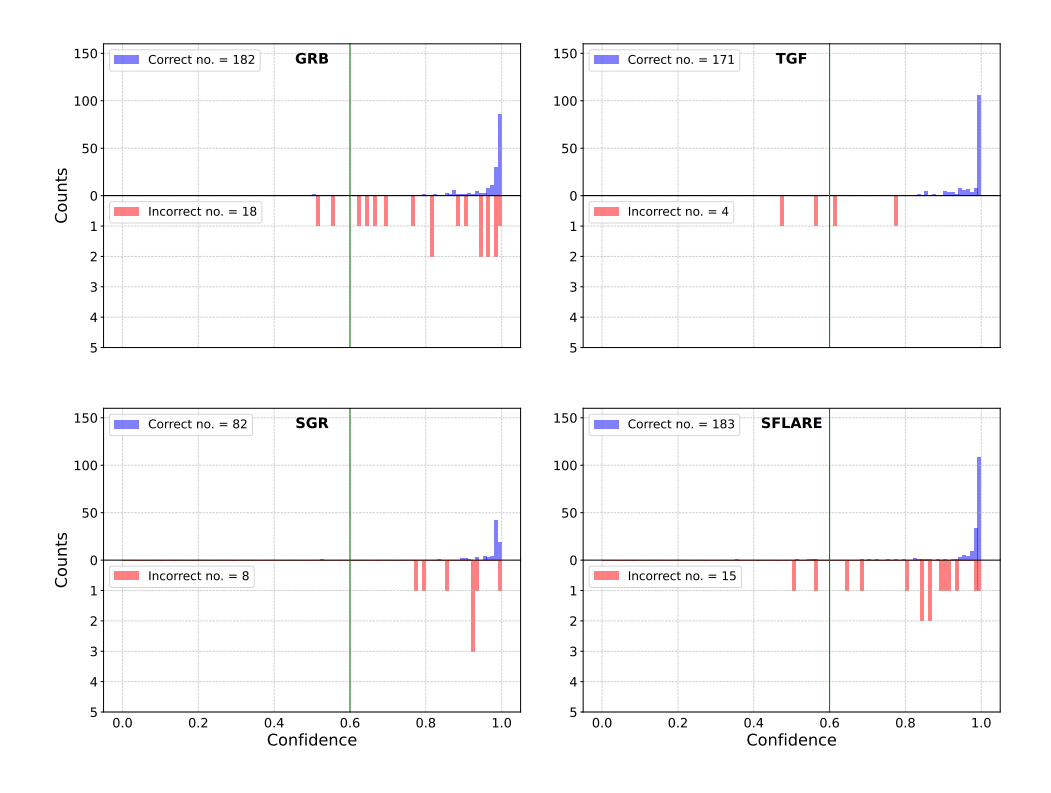


Figure 11: The confidence distributions for all four classes obtained from the R-ConvNet and MI-DCL models are shown in the upper (a) and lower (b) panels, respectively. In each plot, the upper histogram (blue) represents the confidence values for correctly classified data, while the lower histogram (red) corresponds to misclassified data.